Ⓔ

The Use of Direct Shear Waves in Quantifying Seismic Anisotropy: Exploiting Regional Arrays

by Tuna Eken[*] and Frederik Tilmann[†]

Abstract   To overcome the potential contamination of the direct S waves by source-side anisotropy in shear-wave-splitting analysis, we describe a new approach that we call the reference station technique. The technique utilizes direct shear waves recorded at a station pair and depends on maximizing the correlation between the seismic traces at reference and target stations after correcting the reference station for known receiver-side anisotropy and the target stations for arbitrary splitting parameters probed via a grid search. The algorithm also provides a delay time between both stations caused, for example, by isotropic heterogeneities. Synthetic tests demonstrate the stability of the estimated parameters, even where variability in near-surface properties (thickness and velocity of sediment layer) exists. We applied the reference station technique to data from seismic experiments at the northern margin of Tibet. Average splitting parameters obtained from the analysis of direct S-wave results are consistent with those obtained from previous SKS splitting measurements. Where differences exist, shear-wave fast polarization estimates resolved from direct S indicate a higher degree of internal consistency for closely spaced stations than those derived from SKS. This is probably due to the much larger number of direct S waves available for splitting measurements compared to SKS for the same observational period, resulting in higher quality measurements. We also demonstrate the ability of the technique to provide improved splitting measurements for temporary stations by following a bootstrap approach in which only a few stations with well-constrained SKS splitting parameters are used as seeds to determine the splitting parameters of a large array in an iterative manner. In addition, the S measurements sample the anisotropic layer with different angles of incidence and back azimuths, thus potentially providing additional constraints on more complicated anisotropic structures, and the interstation delay times could be used for tomographic studies to reduce the bias from anisotropic structure.

Online Material: Multisplit software package (C++) with instructions.

Introduction

When shear waves propagate through anisotropic media they split into two quasi shear waves—fast and slow. An interference between the fast and slow phases results in elliptical particle motion. If the original (unsplit) S wave is linearly polarized and the waves are affected only by a zone of consistent anisotropy, then the recorded S wave can be rotated such that two very similar phases, apart from scaling and a simple time delay, are seen on the orthogonal components. These orthogonal phases cannot be expected to be exactly identical, because of noise, interfering phases, the effect of near-receiver structure, and the effect of the free surface, but they are often very similar. The orientation of the fast axis controls the rotation angle, and the time delay between the phases corresponds to the product of the strength of anisotropy and the thickness of the anisotropic layer. In most tectonic environments, these parameters predominantly carry information about the mineral orientation of mantle material. Anisotropy due to aligned minerals is thought to be limited to the upper mantle where plastic deformation occurs via dislocation creep (e.g., Karato, 1993; Savage, 1999). However, the S waveform carries no information on where along the path the splitting was acquired, so at teleseismic distances there is ambiguity whether observed splitting is acquired in the mantle below the source (source-side splitting) or below the station

---

*Now at the Department of Geophysical Engineering, the Faculty of Mines, Istanbul Technical University, 34469 Maslak, Istanbul, Turkey.

†Also at Institute of Geological Sciences, Department of Earth Sciences, Freie Universität, Malteserstr. 74-100–Haus H, 12249 Berlin, Germany.

(receiver-side splitting). For this reason, core-refracted shear waves (*SKS* or *SKKS*) are one of the most popular tools for investigating seismic anisotropy (e.g., Kind *et al.*, 1985; Vinnik *et al.*, 1989; Özalaybey and Savage, 1995; Silver, 1996; Savage, 1999; Plomerová *et al.*, 2002; Babuška *et al.*, 2008) at lithospheric scale. These phases are initially polarized as *S* waves at the source, where they can be split, if the crust and mantle below the source is anisotropic. At the core–mantle boundary, the *SV* component of the *S* wave is (partially) converted into a *P* wave, whereas the *SH* energy undergoes total reflection. The *P* wave is again (partially) converted back to an *S* wave on leaving the core and re-entering the mantle beneath the receiver. The outer core thus acts as a polarization filter that removes any source-side splitting. Therefore, the measurement of shear-wave splitting with *SKS* waves allows the isolation of receiver-side anisotropy. In this paper, we are concerned with measuring splitting from teleseismic direct *S* waves instead. In this context, we use an extended definition of source-side splitting to not only mean splitting acquired in the upper mantle near the source but also splitting that might be acquired near the turning point, for example in an anisotropic D″ layer (Maupin *et al.*, 2005; Long, 2009).

The various techniques for evaluating fast polarization direction and splitting time delay (hereafter referred to as FPD and TD, respectively) include eigenvalue maximization, transverse energy minimization, and cross-correlation approaches (Vinnik *et al.*, 1989; Silver and Chan, 1991; Savage and Silver, 1993; Levin *et al.*, 1999). Most of the techniques are based on the idea of recovering the particle motion of the initial shear waves, which in the case of the core–mantle refracted shear waves (e.g., *SKS*) is a linear radial (*SV*) polarization in the ray-path plane. A correction for anisotropy and some side effects is achieved by rotating the horizontal components into a coordinate system aligned with a putative FPD and applying an appropriate time shift to the orthogonal polarization components. The cross-correlation approach aims at detecting the maximum similarity between tentative fast and slow components (Iidaka and Niu, 1998; Levin *et al.*, 1999). Another approach minimizes the ratio of the eigenvalues of the covariance matrix eigenvectors obtained from horizontal components (Silver and Chan, 1988). Several further developments of the methods mentioned above are in use. For instance, the multievent approach developed by Wolfe and Silver (1998) combines data from events approaching from various directions. This method aims at computing the best solution under the assumption of a single anisotropic layer with a horizontal fast axis. Chevrot (2000) introduced splitting intensity estimations as an additional measure of the anisotropy by analyzing the back-azimuthal variations of shear-wave data to examine dipping or multiple layers of anisotropy. Reviews of methodologies are presented in, for example, Savage (1999) and Fouch and Rondenay (2006). According to Vecsey *et al.* (2008), the transverse energy minimization approach yields more stable solutions than other techniques.

Nevertheless, for shorter temporary deployments often only a very small number of splitting measurements from only one or two azimuths can be obtained. In contrast to *SKS* phases, direct *S* waves sample possible anisotropic structures in the upper mantle with an increased range of incidence angles and back azimuths and are thus advantageous for improving the resolution of the 3D orientation of the anisotropic structure. However, direct *S* waves can already be split by source-side anisotropy, which is not easily separated from the receiver-side splitting we are generally interested in. Previous attempts to measure splitting parameters from direct shear waves depended on either the analysis of deep focus events, which are thought to be free from source-side effects (Savage *et al.*, 1990; Fischer and Yang, 1994; Long and van der Hilst, 2005) or an appropriate correction for source-side anisotropy (Yang and Fischer, 1994; Anglin and Fouch, 2005). However, deep earthquakes are only found in a few selected subduction zones and are possibly subjected to both slab and subslab region anisotropy represented by delay times more than 1 s (Wookey *et al.*, 2002; Di Leo *et al.*, 2012). Thus, ignoring source-side effects for such events can be misleading. In the case of explicit correction the source-side anisotropy needs to be determined explicitly, which is often not possible. The main motivation behind this work is to employ direct shear waves for shear-wave-splitting measurements by using an array approach to be able to cancel the source-side effects.

Standard body-wave tomography studies invert the travel-time delays (deviations between observed travel times and those predicted using an initial Earth model) under the assumption of an isotropic Earth. The effect of seismic anisotropy in this case can introduce biases that may lead to improper magnitudes and localization of true model heterogeneities (Lloyd and van der Lee, 2008; O'Driscoll *et al.*, 2011; Eken *et al.*, 2012). Lloyd and van der Lee (2008) reported that the largest amount of this effect could be up to 0.12 s for shear-wave tomography beneath North America. This corresponds to ∼15% of the average splitting time delay (∼1 s) measured beneath cratonic areas (Becker *et al.*, 2012).

In the present study, we describe a new array-based approach for measuring splitting parameters from direct shear waves as well as interstation delays. Our new approach depends on measuring splitting parameters of a station of interest (target station) using a second station (reference station) with a presumed knowledge of anisotropy, which could be obtained, for instance, from conventional *SKS* splitting measurements. For example, the reference station could be a permanent station with well-constrained splitting parameters, and the target station could be part of a temporary array. We first test the validity of our method for various cases in which anisotropy and heterogeneity parameters of a set of hypothetical models vary. Second, we apply the methodology to the INDEPTH IV array in Northeastern Tibet (Zhao *et al.*, 2011; Liang *et al.*, 2012).

Reference Station Methodology

Our approach depends on comparing the anisotropy-corrected direct *S*-wave signals recorded at two horizontal
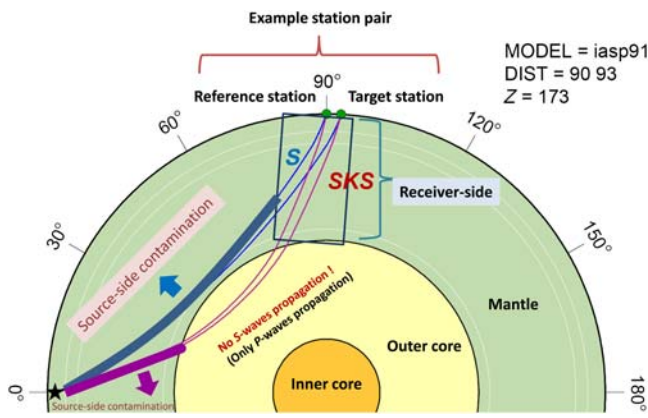
Figure 1. Cartoon illustration depicting theoretical source-to-receiver ray paths of both direct *S*- and *SKS* phases calculated for a station pair with an interstation station distance of 3°. The epicentral distance of the synthetic event, which is assumed to occur at a depth of 173 km, is 90° to the closest station. The color version of this figure is available only in the electronic edition.

components of a reference station with those recorded at a station of interest (referred to as the target station hereafter). The underlying assumption is that source-side splitting affecting both stations are considered to be the same (Fig. 1) and that the splitting effect dominates the shear-wave response. *A priori* knowledge of receiver-side anisotropy of the reference station is usually taken from previous *SKS* splitting measurements.

We analyze two orthogonal horizontal components at a reference station

$$s_R(t) = \begin{pmatrix} n_R(t) \\ e_R(t) \end{pmatrix},$$

in which $n_R(t)$ and $e_R(t)$ are the north and east component time series, and a target station

$$s_T(t) = \begin{pmatrix} n_T(t) \\ e_T(t) \end{pmatrix}.$$

The first step is the correction for receiver-side anisotropy beneath the reference station by applying a backward angular rotation and time shift on the reference traces of the horizontal components using the inverse of the assumed known anisotropic parameters at the reference station ϕ_R (FPD) and δt_R (TD):

$$s'_R(t) = \Gamma^{-1}_{\phi_R, \delta t_R} s_R(t) = \Gamma_{\phi_R + \pi/2, \delta t_R} s_R(t),$$

in which $\Gamma_{\phi, \delta t}$ is the forward splitting operator with FPD ϕ and TD δt, and Γ^{-1} its inverse, identical to the forward operation with fast and slow axis exchanged. After the correction, the new signal at the reference station should represent only source-side anisotropy, which is also assumed to be identically present within the signal recorded at the target station. Then in the next step, a grid search is carried out

for the FPD and TD at the target (ϕ_T and δt_T), which provide the highest similarity between the reference and target station signals. The inverse splitting operator is applied to the trial values to obtain a corrected target trace:

$$s'_T(t) = \Gamma^{-1}_{\phi_T, \delta t_T} s_T(t).$$

For each value of ϕ_T and δt_T, a time shift Δt and amplitude factor a are also optimized to account for travel-time differences caused by lateral heterogeneities and the differences in site response, respectively. The misfit surface is defined by the residual energy that is obtained by subtracting corrected waveforms at reference and target stations:

$$
\begin{aligned}
E(\phi_T, \delta t_T) &= \int_{t_1}^{t_2} \|2(a s'_T(t + \Delta t) - (1 - a) s'_R(t))\|^2 dt \\
&= 4 \int_{t_1}^{t_2} [(a n'_T(t + \Delta t) - (1 - a) n'_R(t))^2 \\
&\quad + (a e'_T(t + \Delta t) - (1 - a) e'_R(t))^2] dt,
\end{aligned}
$$

in which t_1 and t_2 are the limits of the analysis window (reference and target traces are assumed prealigned, for example, according to the theoretical *S* arrival time); $a = 0.5$ corresponds to no amplitude correction, $a > 0.5$ if the observed amplitude at the target station is larger than at the reference station, and $a < 0.5$ if the amplitude of the target traces is less than those of the reference traces. No explicit grid search needs to be carried out for Δt and a. Δt is the time lag, which maximizes the sum of the cross-correlation functions between the reference and target stations for two orthogonal components.

$$CC(t) = (n'_R * n'_T)(t) + (e'_R * e'_T)(t),$$

in which asterisk (*) is the cross-correlation operator such that:

$$(n'_R * n'_T)(t) = \int_{t_1}^{t_2} n_R(\tau) n_T(\tau + t) dt.$$

The two-component cross-correlation function CC is invariant with respect to rotations of the horizontal components, such that for computational convenience it can also be calculated based on the time-shifted fast and slow components. a is given by the explicit expression

$$a = \frac{E_R + CC(\Delta t)}{E_R + 2CC(\Delta t) + E_T} \quad \text{with}$$

$$E_R = \int_{t_1}^{t_2} [n_R(t)^2 + e_R(t)^2] dt,$$

$$E_T = \int_{t_1}^{t_2} [n_T(t + \Delta t)^2 + e_T(t + \Delta t)^2] dt.$$

By precalculating two-component cross-correlation matrices, an efficient implementation of the grid search is

possible, whereby $E(\phi_T, \delta t_T)$, Δt, and a can be determined for each set of splitting parameters without recalculating cross-correlation functions by applying appropriate rotations and time shifts to the precalculated matrices.

The minimum residual energy $E(\phi_T, \delta t_T)$ represents the maximum similarity between the corrected signals, and the corresponding values of ϕ_T and δt_T define the estimate of FPD and TD for receiver-side anisotropy at the target station. In the actual implementation, the residual energy is normalized by the energy available in the input time series, that is, $E(\sigma_T, \delta t_T)/\sqrt{E_R E_T}$. Unlike in classic splitting measurement methods, the corrected traces are not necessarily linearly polarized but might carry the signature of splitting near the source. The isotropic time delay Δt and amplitude correction factor a are by-products of the procedure, and the detected time delays could be useful as input for tomographic inversions unbiased by polarization anisotropy. Our method requires stations spaced sufficiently closely that the initial polarization at the source and the source-side splitting can be assumed to be identical for both stations. This assumption will usually hold for teleseismic events recorded at regional temporary arrays with the station spacing of up to a few tens of kilometers.

Testing the Methodology: Synthetic Examples

To demonstrate the algorithm and test the validity of our assumptions, and their sensitivity to various structural variations not accounted for explicitly (e.g., sedimentary layer thickness, abrupt changes in the Moho topography, etc.), we conducted several synthetic tests. For all synthetic tests, anisotropic layers are arranged to have a fast symmetry axis in the horizontal plane. To generate synthetic waveforms, we used the technique developed by Frederiksen and Bostock (2000), which is based on a high-frequency asymptotic method without requiring any ray tracing.

Simple Model

In the first test, we started with a hypothetical setup where receiver and target stations are separated by 0.5° interstation distance. Under both stations a 35 km thick isotropic crust overlies a 250 km mantle layer with azimuthal anisotropy (Fig. 2a). Isotropic *P*- and *S*-wave velocities (V_P and V_S) are the same under both stations, but the FPDs in the anisotropic layer beneath receiver and target stations differ by 5°. As we just model the receiver response with a prescribed slowness based on the event depth and epicentral distance, we need to simulate source-side anisotropy by introducing another anisotropic layer, the FPD of which is the same for both stations, underlain by an also identical isotropic half-space. We model a teleseismic event at 200 km depth, a back azimuth of 180° and 72° and 72.5° epicentral distance from the reference station and target station, respectively, which is assumed to radiate pure *SV* in the direction of the stations. The resulting waveform is presented in Figure 3a,c; even though the data are

noise-free synthetics the waveform is more complicated than the simple elliptical waveform expected for single-layer splitting due to the presence of source-side splitting. Normally, we would not know the correct splitting parameter at this stage, but with hindsight, or based on our knowledge of the true model, we can rotate the seismograms into the fast/slow direction (Fig. 3e); again where the fast and slow waveforms are not identical as would be expected for a single anisotropic layer and in the absence of source-side splitting. After correcting for the time delay (Fig. 3g), the receiver-side splitting has been removed and the corrected traces carry only the source-side splitting. To find the optimal FPD and TD at the target station, we need to have *a priori* information about the splitting at the reference station, for example, from *SKS* observations. We then correct the reference waveform for the known splitting (Fig. 3a). The target waveform (Fig. 3c) is then corrected for all possible trial FPDs and TDs according to the grid-search limits. The residual energy is calculated by subtracting the corrected reference and target waveforms from each other, after application of an additional time shift and amplitude factor, and summing the amplitudes of the residual trace. Figure 3m shows the resulting residual energy surface, which shows a sharp minimum at the correct splitting parameters for the target station. The corresponding corrected target waveform and residual traces are shown in Figure 3i,j and 3k,l, respectively. The reference station algorithm estimated the FPD within 2° of the true FPD beneath the target station (Fig. 3m). The residual trace is not exactly zero because the algorithm does not take into account crustal reverberations or the small difference in angle of incidence between the arrivals at both stations. For the same reason, the amplitude factor differs by 1.6% from the expected value of 0.50. In this example, the time shift results from the different epicentral distance and associated travel-time difference, but in a realistic setting it would also carry information about lateral heterogeneity.

Models with Varying Crustal Thickness and Velocities

In reality, the observed waveform differences between reference and target stations result not only from different anisotropic structures, but also from lateral heterogeneity, in particular crustal structure. To estimate to what degree these variations degrade the anisotropy measurements, we test models with the same model parameters as in the Simple Model section except for up to 20 km difference between the Moho depths beneath receiver and target stations (Fig. 2b). Applying the algorithm to the forward-modeled waveforms resulted in a deviation of 2° between the measured FPD and the true FPD for the 55 km thick crust at the target station. Examples of synthetic waveforms, the residual energy surface, and optimal residual traces that were obtained after applying the reference station technique in this case can be found in Figure 3b,d,f,h,j,l,n. A systematic test using various target station models (Fig. 2c) the crustal thicknesses of
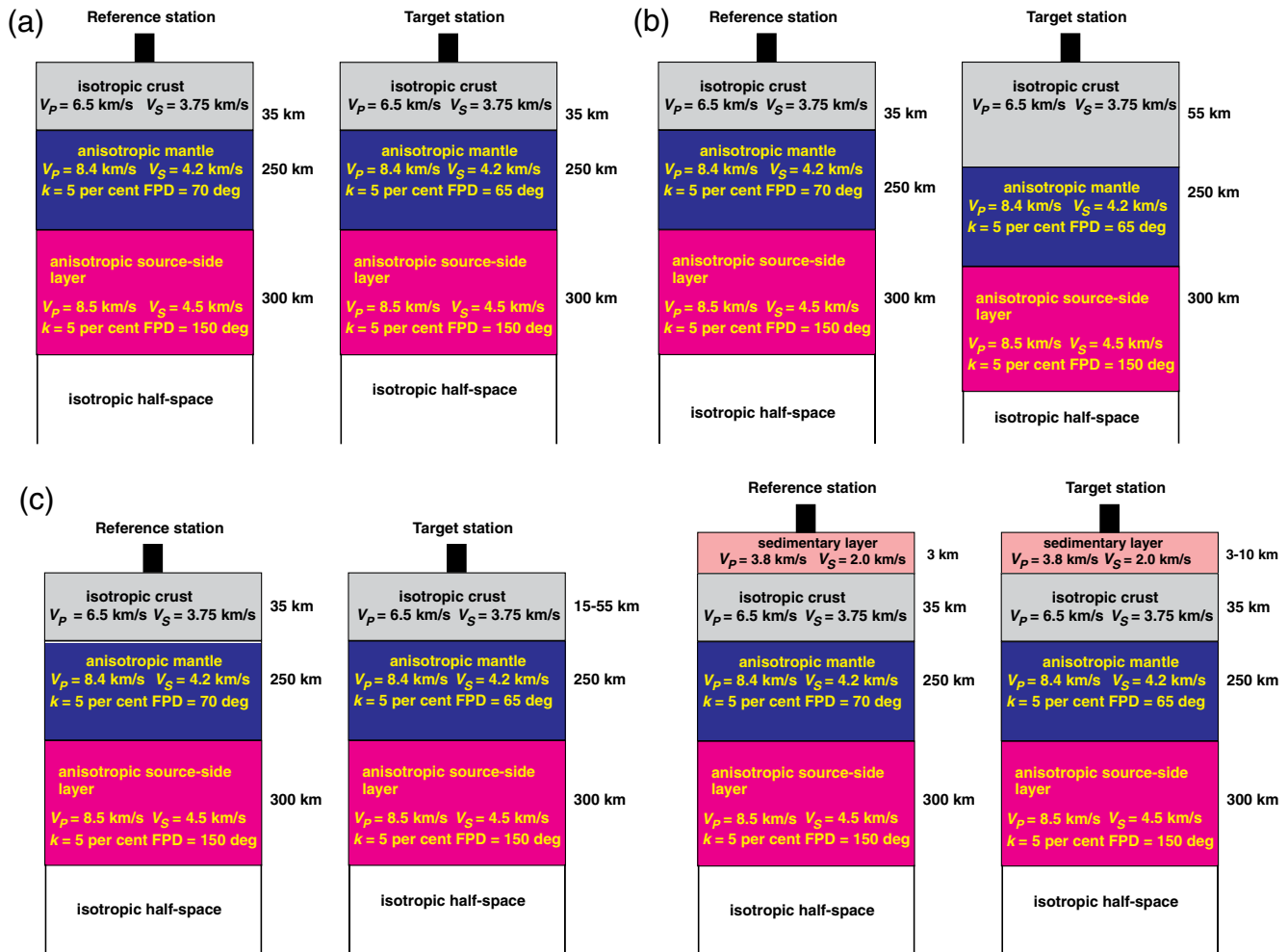
Figure 2. Configuration of various models used for synthetic tests (not to scale). (a) Represents a simple model in which target and reference stations are located on almost the same type of crustal and lithospheric structure. The only difference between them is a 5° difference in the fast polarization direction (FPD) within the second layer from the top. (b) In addition to the 5° difference in FPD, the crustal thickness of the reference and target stations differs by 20 km. (c) depicts models used for the synthetic tests performed to understand the influence of varying crustal thicknesses (two left panels) and sedimentary layer thickness (two right panels) beneath the target station. The color version of this figure is available only in the electronic edition.

which range from 15 to 55 km has resulted in deviations of not more than 3°, suggesting even quite pronounced crustal thickness variations underneath the seismic array would not have a systematic and drastic impact on the estimation of anisotropy parameters (Fig. 4a,b).

The Effect of Sediments

Sediments may reach a thickness of ~5 km and more in some regions (e.g., Qaidam Basin [QB], northeast China; Black Sea, northeast Turkey, etc.), and their thickness can vary sharply at basin edges. Because of the strong contrast in seismic properties of sediment and basement, they exert an even more important influence on waveform characteristics than crustal thickness variations. Therefore, we tested a series of models that were similar to the simple model described in the Simple Model section, but for both reference

and target stations a sedimentary layer now overlies the crust (Fig. 2c). With an identical sedimentary thickness of 3 km below reference and target stations, a 2° deviation with respect to the true anisotropic model was observed. As the sedimentary layer thickness of the target station differs from that of the reference stations (Fig. 2c), we observe deviations of estimated and true FPDs from between −4° and 1° (Fig. 4d). Resultant synthetic waveforms corresponding to varying sedimentary layer thickness ranging between 1 and 10 km can be seen in Figure 4c. Although the structural effects are therefore not entirely negligible and need to be kept in mind, in general the deterioration of the measurement accuracy is probably comparable to the effect of random noise on *SKS* measurements in most cases. Further mitigation results from the averaging of many measurements with different reference stations for any given target station (see the next section).
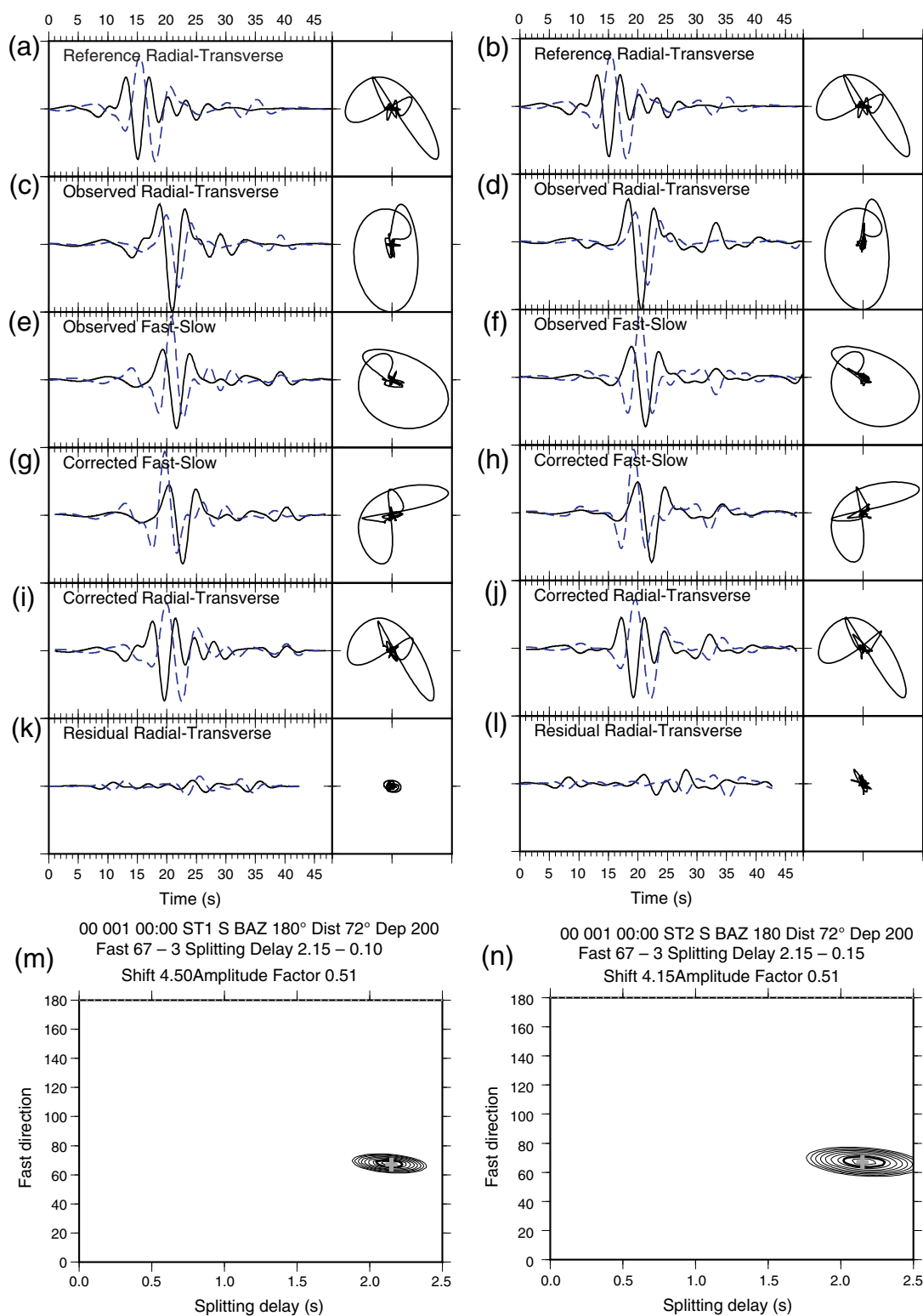
Figure 3. Two examples of *S*-wave splitting estimation derived using the reference station technique performed with synthetic data. Figures on the left panel represent application of the method to the simple synthetic case presented in Figure 2a. (a) Signals at reference station with receiver-side correction, (c) signals at target station, (e) fast and slow components after rotating signal at target station using optimum FPD (67°), (g) fast and slow components corrected for splitting delay (2.15 s), (i) corrected radial and transverse components at target station using optimum splitting parameters and isotropic delay (4.50 s), (k) residual trace, (m) indicates the misfit surface with a well-defined minimum at splitting parameters 67° ± 3° and 2.15 ± 0.1 s. Figures on the right panel show the same procedure obtained from the application of the method to the synthetic case presented in Figure 2b. Note that synthetic seismograms belonging to the same event are all plotted to the same scale. The color version of this figure is available only in the electronic edition.
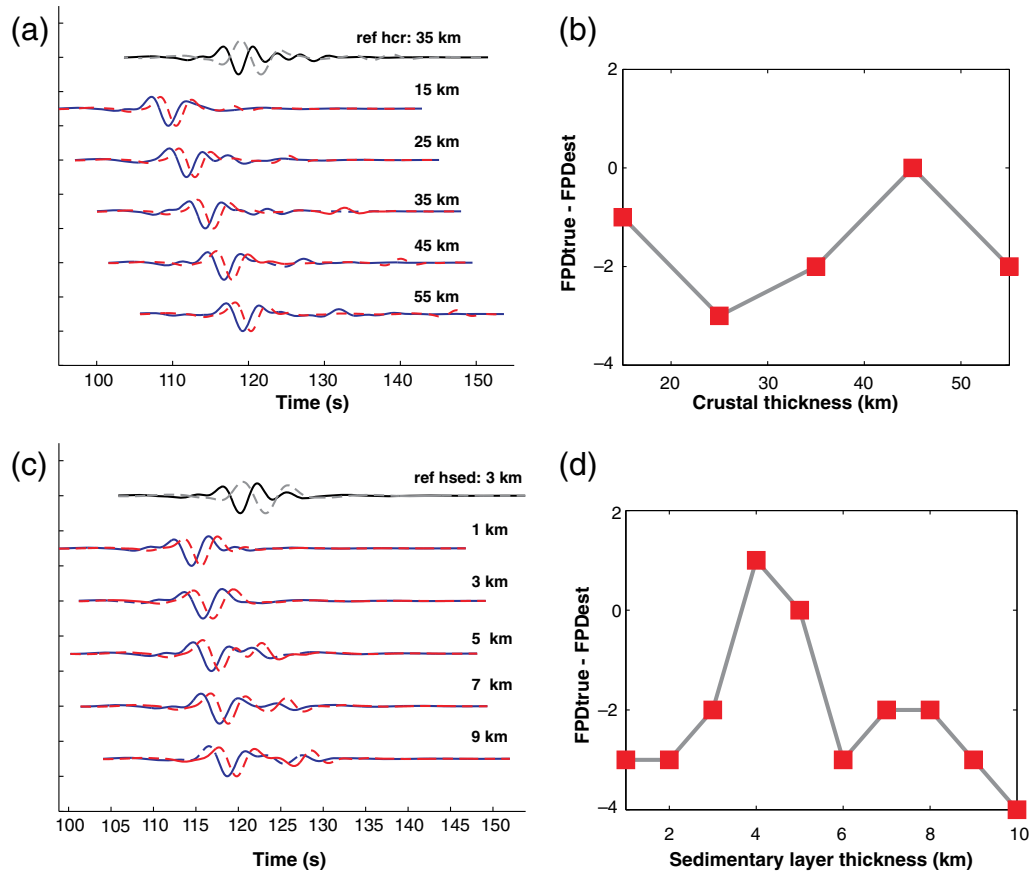
Figure 4. (a) Synthetic waveforms for the varying crustal thickness test generated at the reference station and target stations (solid line north–south and dashed line for east–west component). Signals at reference and target stations are generated based on the model presented in Figure 2c. "ref hcr" denotes the crustal thickness (35 km) beneath the reference station whereas 15, 25, 35, 45, and 55 km indicate the range of crustal thickness beneath the target station. (b) The resulting deviations of the estimated *S*-derived fast polarization azimuths from the true model when the crustal thickness varies beneath the target station. (c) Synthetic waveforms for the varying sedimentary layer thickness test generated at reference station and target stations (solid line for north–south and dashed line for east–west component). Signals at reference and target stations are generated based on the model presented in Figure 2c. "ref hsed" denotes the sedimentary layer thickness (3 km) beneath the reference station. The range of sedimentary layer thickness beneath the target station is from 1 to 10 km. Here, we only show five waveform examples that are generated for 1, 3, 5, 7, and 9 km of sedimentary layer thickness. (d) The resulting deviations of the estimated *S*-derived fast polarization azimuths from the true model when the sedimentary layer thickness varies beneath the target station. The color version of this figure is available only in the electronic edition.

Application to Northeast Tibet

Study Area

Following the synthetic tests, we applied our method using teleseismic direct *S*-wave observations recorded at the temporary seismic stations of the INDEPTH IV linear array and the areal ASCENT network extending over almost the entire northeastern part of the Tibetan Plateau. The aim of these experiments was to study how continental collision is accommodated in the crust and mantle at the northern margin of the plateau. This area is suitable as a test region for this study because it represents an example of a relatively dense regional array, for which *SKS* splitting measurements have already been carried out, which can serve as references as well as being available for comparison (Leon-Soto *et al.*, 2012; Eken *et al.*, 2013). The *SKS* measurements show some variability but generally follow a large scale pattern, making

it easier to assess the plausibility of the measurements using the new method.

Dataset

A total of 82 seismic stations with average *SKS* splitting measurements available were used in this work. Forty two of these stations (shown in white circles in Fig. 5) belong to a linear array that was deployed during the INDEPTH IV experiment. The linear array was operated from 30 May 2007 to 6 September 2008 and crosses from the northernmost part of the Qiangtang Terrane (QTGT) across the Jinsha Suture to the Songpan Ganzi Terrane and then ends at the southern edge of the Qaidam Basin, covering an area that includes major fault zones such as the north and south Kunlun faults (NKF and SKF) and the north Kunlun thrust (NKT; Fig. 5). The sampling rate for these sets of stations is 50 samples per second. The 40
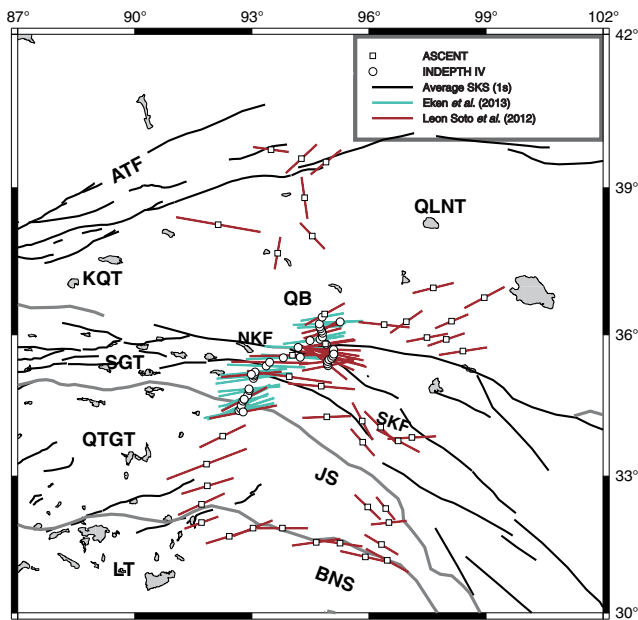
Figure 5. Map of the study area with all stations utilized in this work and their corresponding station average *SKS* splitting parameters taken from León Soto *et al.* (2012) and Eken *et al.* (2013). Time delay of 1 s is represented by black bar in the legend. In the map, suture zones are shown by gray lines whereas left-lateral strike-slip faults are represented by black lines. LT, Lhasa Terrane; QTGT, Qiangtang Terrane; SGT, Songpan-Ganzi Terrane; JS, Jinsha Suture; BNS, Bangong-Nujiang Suture; KQT, Kunlun-Qaidam Terrane; QLNT, Qilian Terrane; QB, Qaidam Basin; SKF, South Kunlun Fault; NKF, North Kunlun Fault; and ATF, Altyn Tagh Fault. The geologic dataset used in this map is based on Taylor and Yin (2009). The color version of this figure is available only in the electronic edition.
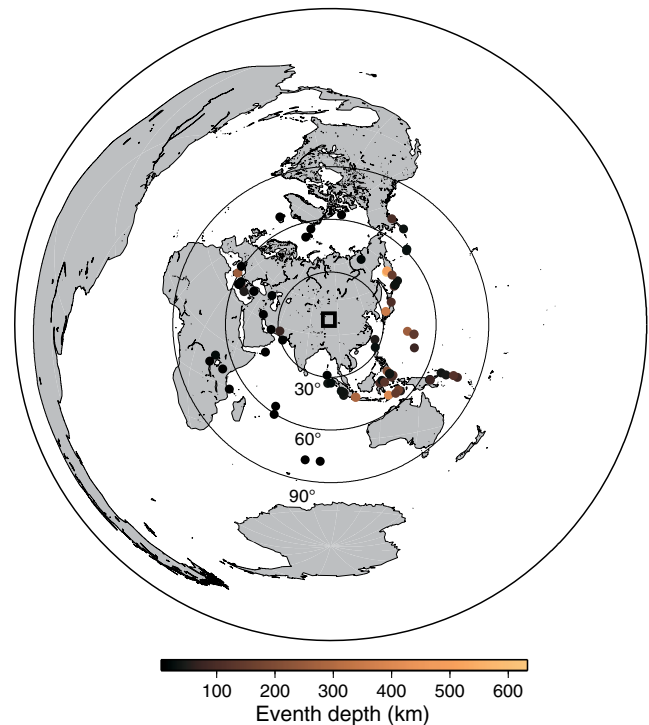

Figure 6. Epicentral distributions of 77 teleseismic events with direct *S* waves signal used in this study (rectangle). The large circles indicate epicentral distances of 30°, 60°, and 90°. The color version of this figure is available only in the electronic edition.

temporary broadband stations from the ASCENT-2D array were operated from May 2007 to June 2009 and recorded with a sampling rate of 25 samples per second. The 2D array covers an area including the Qiangtang and Songpan Ganzi Terranes and the Kunlun Mountains between about 92° and 97° E. Sparse stations are also found further north in the Qaidam Basin and in southern Qilian Shan (Fig. 5).

The event selection, which was optimized to provide sufficient azimuthal coverage, is taken from a previous teleseismic tomography study (Nunn *et al.*, 2014). We used 15,297 waveforms of direct *S* waves extracted from 77 teleseismic events with epicentral distances ranging between 25° and 80° and magnitudes ranging between 5.2 and 6.9 (Fig. 6). Hypocentral depths of these teleseismic events range from 6 to 632 km. The spatial variation of hypocentral depths is presented in Figure 6. Prior to data analysis, the instrument responses were removed from the original seismograms. At the final stage of preprocessing, all seismograms were filtered with a bandwidth of 0.03–0.2 Hz. Figure 7 shows an example record section displaying some selected band-pass filtered waveforms with *S* arrivals.

Data Analysis

We started by determining station pairs over the entire area. Among 7122 possible station pairs, we selected 2732

with interstation spacing less than 300 km (pairs of the same stations where the roles of target and reference stations are exchanged are counted as separate). We can apply the reference station technique on a station pair when four horizontal components recorded at two stations are available for a given earthquake. Thus, the ideal number of station pairs is not reached for each event because combining two different arrays with different operational time periods often caused one station of a pair to have no data. Because event waveforms used in this work formed the dataset of a previous tomography study, we started with using waveforms of *S* signals that were already selected after a visual inspection by eliminating low-quality waveforms. A set of automatic criteria to select the final splitting parameters (see below) also functioned as a second tool to avoid noisy data. Finally, a total of 98,012 waveform pairs could be found from 77 events. Our dataset has provided 1272 and 2401 station pairs per event as the average and maximum values, respectively.

The *a priori* information on receiver-side seismic anisotropy, which will be used for signal correction, was compiled from the *SKS* splitting measurements performed by Leon Soto *et al.* (2012) and Eken *et al.* (2013). Both studies use the minimum tangential energy minimization method (Vinnik *et al.*, 1989; Silver and Chan, 1991; Savage and Silver, 1993). After correcting the signal at a reference station for receiver-side anisotropy, we performed the reference station technique described in the Testing the Methodology: Synthetic Examples
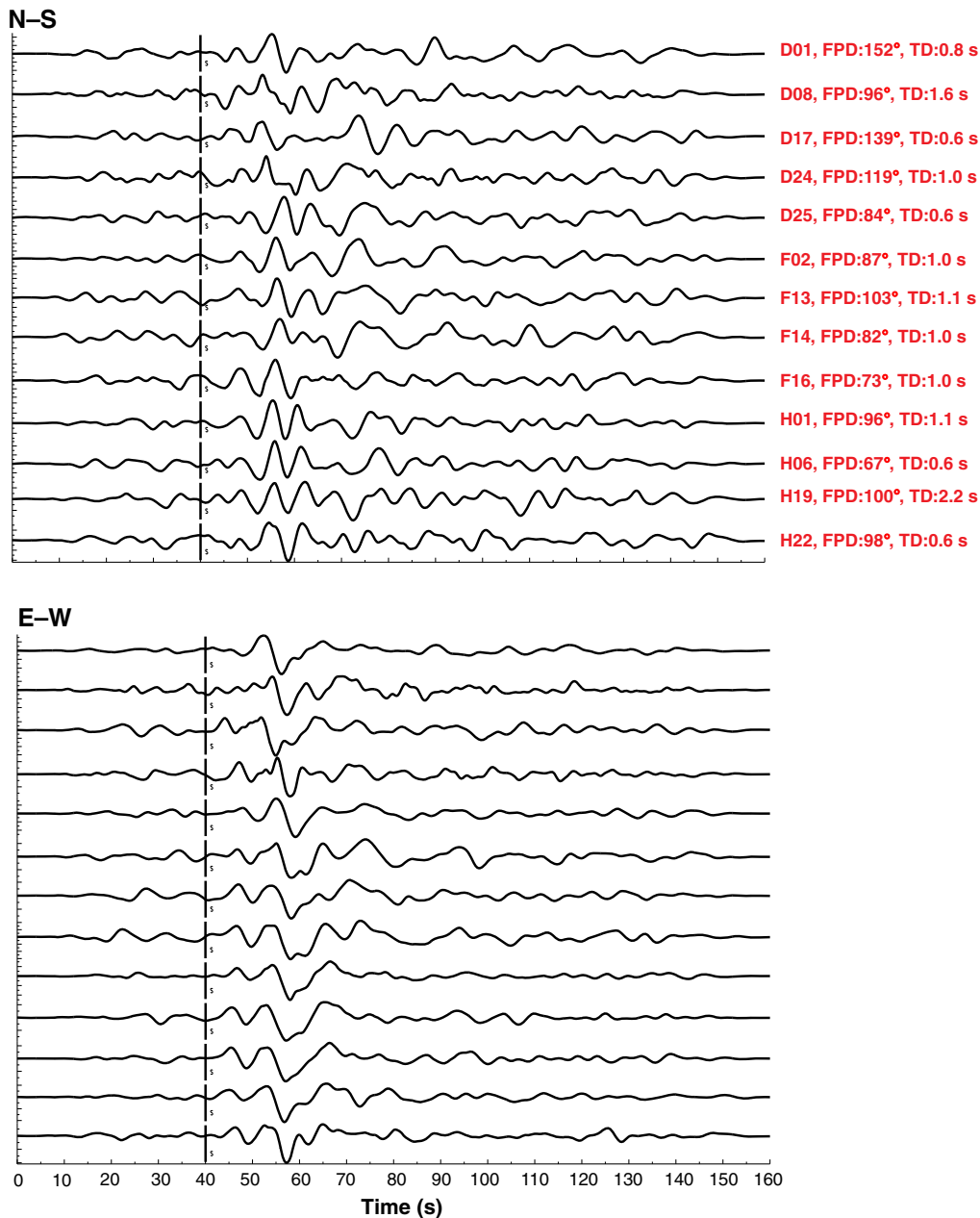
EventID: 2008329090258

N–S

D01, FPD:152°, TD:0.8 s
D08, FPD:96°, TD:1.6 s
D17, FPD:139°, TD:0.6 s
D24, FPD:119°, TD:1.0 s
D25, FPD:84°, TD:0.6 s
F02, FPD:87°, TD:1.0 s
F13, FPD:103°, TD:1.1 s
F14, FPD:82°, TD:1.0 s
F16, FPD:73°, TD:1.0 s
H01, FPD:96°, TD:1.1 s
H06, FPD:67°, TD:0.6 s
H19, FPD:100°, TD:2.2 s
H22, FPD:98°, TD:0.6 s

E–W

Time (s)

Figure 7. Examples of the north–south (top) and east–west (bottom) component data for the event of 24 November 2008 09:02 recorded at thirteen stations, epicenter 54.20° N, 154.32° E, magnitude 6.5, epicentral distance 45° (great circle arc length) to the center of the network. Traces are aligned according to theoretical S arrival times in the IASP91 (shown by vertical lines). Station averaged *SKS*-derived FPDs and TDs at each station to be used for receiver-side anisotropy correction is given next to the north–south component of each trace. The color version of this figure is available only in the electronic edition.

section to each seismogram pair. We used a 45 s analysis window starting 15 s prior to the theoretical S-wave onset. The time-window length was chosen to minimize the effect of coda waves and contamination by converted phases. This window length was adopted after synthetic tests because it excluded crustal S multiples in the thick Tibetan crust as an undesired influence. For the grid search, horizontal com-

ponents were rotated from 0° (west) to 180° (east) in 1° increments and shifted for splitting time delays ranging from 0 to 3.5 s in 0.05 s increments. The time shift Δt is not allowed to exceed 5 s after records have been prealigned according to the theoretical travel-time prediction. Figure 8m shows an example measurement with a well-defined minimum in the residual energy surface. Whereas the observed uncorrected

target waveform looks very different from the reference station waveform (Fig. 8a,c), the corrected waveform is much more similar (Fig. 8a,i). The residual trace is dominated by random noise although the peak in the transverse component at ~25 s in the residual trace (Fig. 8k) hints at some minor waveform effect, which cannot be explained by single-layer anisotropy.

An uncertainty analysis of the resolved splitting parameters was achieved through the inverse *F*-test error analysis following Silver and Chan (1991). In this, it is tested whether the increase in residual energy away from the minimum represents a significant increase according to the preset confidence level, usually set to 95%. This analysis depends on the number of degrees of freedom in the data and parameters. We set this to one degree of freedom per second for each residual trace, that is, for the two horizontal components the degrees of freedom of the data will be twice the length of the analysis window in seconds following Silver and Chan's observation that this is a typical value for teleseismic data. This number is reduced by the number of adjustable model parameters, that is, four at the minimum point (FPD, TD, isotropic delay, amplitude correction factor), and two at arbitrary values of FPD and TD as isotropic delay and amplitude are optimized for each set of splitting parameters. As the number of degrees of freedom in the time series is hard to estimate, and the underlying assumption that the bandlimited Gaussian noise is not fully justified (e.g., Walsh *et al.*, 2013), the absolute values of the error bounds are indicative only but allow a comparison of the reliability of individual estimates.

In conventional *SKS* splitting studies, very small TD (e.g., < 0.4 s) are often interpreted as null measurements (Fouch and Rondenay, 2006). Null-splitting measurements may arise even for anisotropic structures for selected initial polarization directions of the incoming shear wave: null splitting is measured if the initial polarization direction below the anisotropic layer is parallel to the direction of either the fast or slow axis. Therefore, null-splitting results in a typical misfit surface represented by two minimum residual energy zones elongated in the TD direction, and separated by 90° from each other in the FPD direction; these zones join up with a zone elongated in FPD direction at very small values of TD. Where the actual minimum is found within these elongated zones is determined by details of the random noise, and in particular it can occur at high apparent values of TD. To avoid misinterpreting such measurements, our procedure includes the calculation of residual energy under the assumption of no splitting and then compares this to the residual energy at the actual minimum to determine how strongly the data exclude null splitting in a statistical sense, again using the *F*-test. The estimated null-split rejection criterion thus estimated is used in further steps of the data analysis to eliminate null cases from the splitting measurements. Figure 8b,d, f,h,j,l,n shows an example of a null-splitting measurement. The coherent part of the target waveforms is already fairly similar to the reference waveform, such that no splitting correction is really required (Figs. 8b,d). Furthermore, the radial

trace of the reference waveform carries little or no coherent energy (Fig. 8b). The residual surface accordingly shows the typical pattern with relative lows at FPDs of ~80° and 170°, close to parallel and perpendicular to the initial polarization direction, respectively (Fig. 8n). The nominal minimum is at a TD of 3.5 s (at the limit of the grid search), and a FPD of 167°, but the null rejection test shows that null splitting cannot be rejected with a 95% confidence or more.

Before averaging the results of many individual measurements to find the final splitting parameters for each station, we apply a stepwise quality assessment to ensure the stability of the results. We only considered waveform pairs (1) with normalized minimum residual energy smaller than 0.5; (2) with amplitude correction factor parameter *a* between 0.4 and 0.6; and (3) where null splitting is rejected at 95% confidence level or higher. Criterion (1) is applied to ensure that the assumption of identical source-side splitting and absence of strong scattering phases is approximately satisfied. Criterion (2) allows us to reject results obtained from waveform pairs with strong amplitude differences, which might hint at strong site effects or 3D heterogeneity. Criterion (3) eliminates null-splitting cases, which would not be appropriate to include in a station average. Finally, 9925 out of 99,082 waveform pairs could pass our selection criteria for further interpretation.

Results

Spatial Distribution

In this section, we mainly present station averages of optimum splitting parameters. Station averages were calculated by taking the circular mean of entire direct *S*-wave-derived FPDs and normal mean of the split TDs obtained from the station pairs that fulfill the quality assessment criteria procedure at a given station. We apply Von Mises approach (Cochran *et al.*, 2003) modified to take into account 180° periodicity by calculating the circular mean of the FPDs, $\phi_{T,\mathrm{Mean}}$, as follows:

$$A = \sum_{i=1}^{N} \sin(2\phi_{T,i}),$$

$$B = \sum_{i=1}^{N} \cos(2\phi_{T,i}), \quad \text{and}$$

$$\phi_{T,\mathrm{Mean}} = \frac{1}{2} a \tan 2(B, A),$$

in which N represents the number of observations and $a \tan 2(y, x)$ is equal to $\tan^{-1}(y/x)$ for $x > 0$, but returns angles between 0° and 360° according to the signs of x and y.

Station averaged estimates are obtained in two steps. First, for each event and target station we average measurements obtained at all available reference stations. Second, the estimates based on each event are averaged to obtain the final estimate for the target station. A comparison of optimum
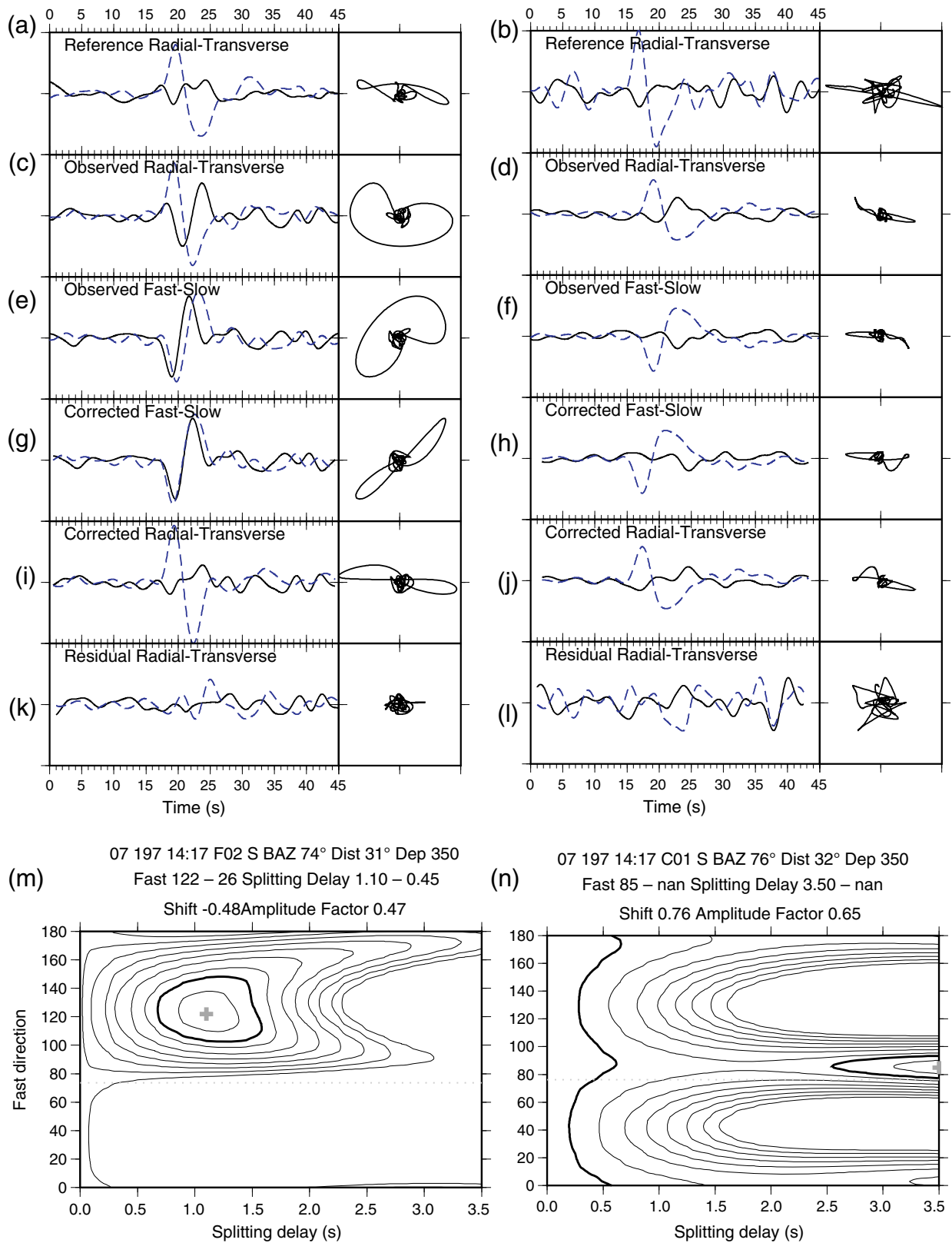
Figure 8. (a, c, e, g, i, k, and m) Reference station technique performed on observed *S* signals recorded at station pair F01–F02. Here, F02 represents the target station the unknown splitting parameters of which are searched for. Explanation for each panel is the same as in Figure 3. (b, d, f, h, j, l, and n) The similar process performed on *S* signals recorded at station pair, A01–C01. This example is selected to show the null-splitting case estimated at the target station C01. Event information is given in the top of the first panel. Note that synthetic seismograms belonging to the same event are all plotted to the same scale. The color version of this figure is available only in the electronic edition.
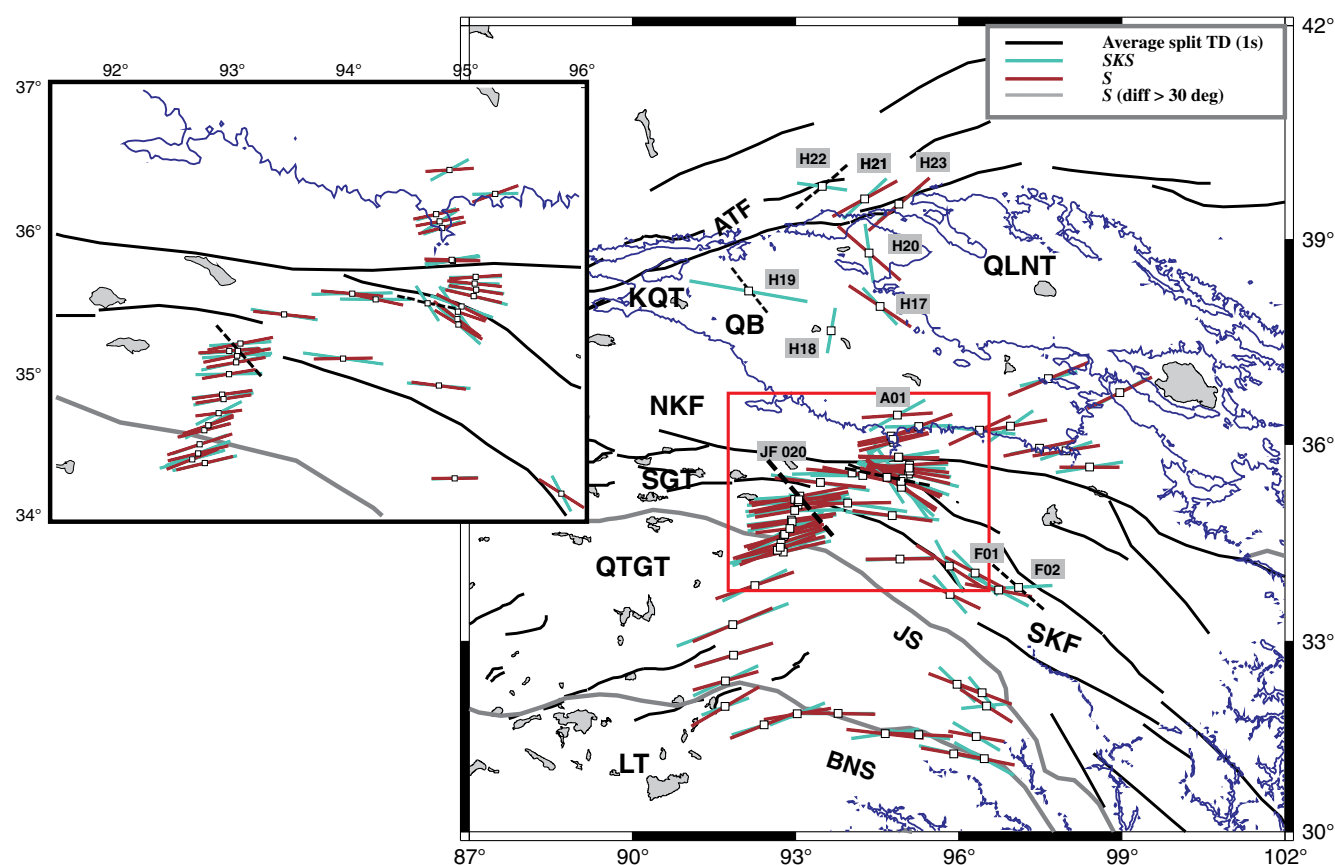
Figure 9. *SKS*- and *S*-waves derived splitting parameters on the map of the study region. The directions (measured from the north) of the solid bars represent the FPD. Solid bar at each station is scaled based on its corresponding TD where 1 s of time delay is represented by the black bar in the legend. The stations with a misfit larger than 30° between station averaged *S*- and *SKS*-derived splitting parameters are highlighted by dashed bars for the *S* measurements. Regions corresponding to an elevation higher than 3000 m are marked in thin contours. Major geologic boundaries (i.e., faults, terranes, suture zones, etc.) and their annotations are the same as those in Figure 5. The color version of this figure is available only in the electronic edition.

splitting parameters estimated from *S* waves through the reference station approach with those estimated using *SKS* arrivals and the minimum transverse energy method provides an opportunity to assess the reference station technique in addition to the synthetic analysis. Figure 9 presents a comparison between the station-averaged fast polarization directions and split delay times obtained from using *SKS* and direct *S* waves plotted over the study area. According to this figure, average results from the application of two different methods to two different wave types, in general, show very good consistency, especially in the region between the northern edge of the QTGT and the NKT (34°–37° N, 91°–99° E). Average FPDs in this region correlate with the trend of major geological features (NKF and SKF) and maximum shear strain as inferred from earthquake focal mechanisms. To the south between the southern part of the QTGT and the upper northern boundary of the Lhasa Terrane (LT; 31°–33° N, 91°–97° E), average FPDs exhibit a curved pattern in which they rotate from northeast–southwest to northwest–southeast directions beneath the eastern Himalayan Syntaxis. For four stations (H17, H18, H19, and H20) located in the northern

part of the study area within the QB average FPDs estimated from direct *S* arrivals are inconsistent with average *SKS* measurements. There, the absolute deviations range from 39° to 81° (Fig. 9). However, average single-event splitting parameters from *SKS* measurements in the basin also showed a more complicated pattern with some back-azimuthal dependency of splitting parameters (León Soto *et al.*, 2012), implying that a more complicated anisotropy pattern, for example, multilayer, prevails here compared to the Tibetan plateau. In the northernmost part of the study area across the Altyn Tagh Fault (ATF), for three stations (H21, H22, and H23), average FPDs obtained from the direct *S* waves are subparallel to the main strike of the ATF and deviations from the *SKS* measurements are relatively small again, indicating that the relative sparsity of stations was not an important factor behind the discrepancies in the QB (Fig. 9).

The differences between *SKS* and *S*-wave derived average splitting parameters are also visualized as scatter plots in Figure 10a,b. The standard deviation of the differences between both methods is 10.3° for the FPDs and 0.2 s for the TDs. Large differences mainly occur if the number of
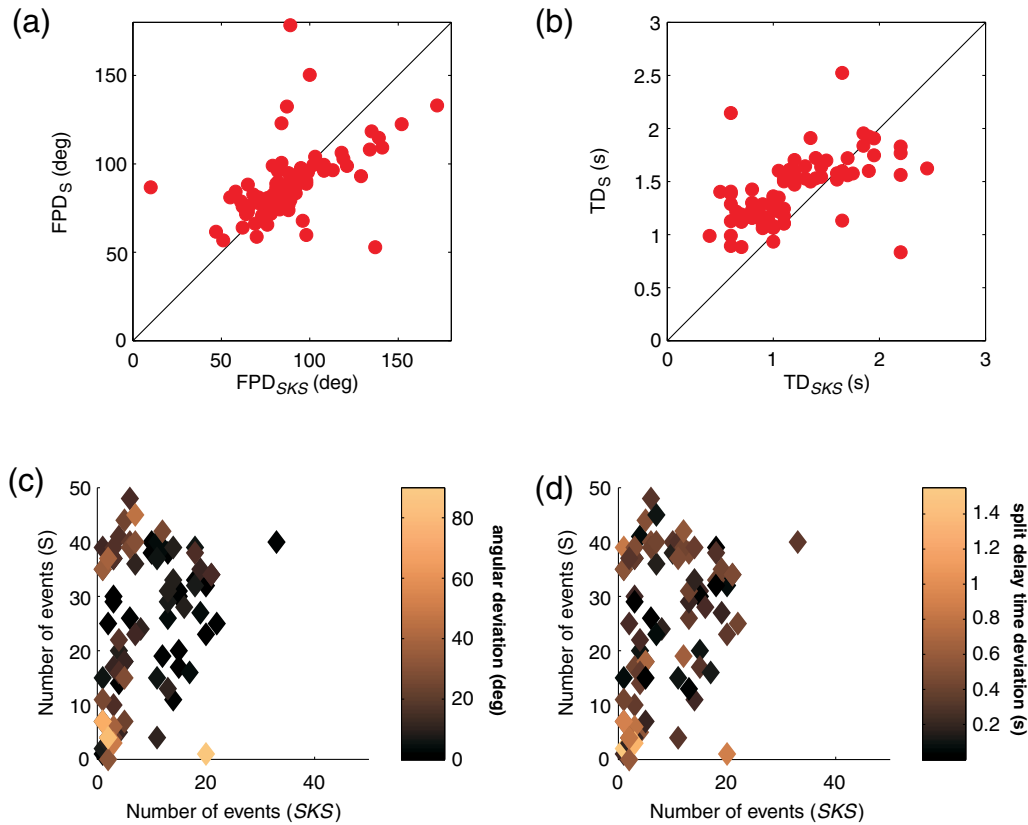
Figure 10. Comparison of the station averaged *SKS*- and *S*-waves derived splitting parameters. (a) and (b) Scatter plots of the station averaged *SKS*- and *S*-waves derived FPD and split TDs, respectively. (c) The number of individual *SKS* splitting measurements versus the number of events used for *S*-wave splitting measurement. Each station in this plot is marked by an absolute deviation value obtained by subtracting the station averaged *S*-derived FPDs from the station averaged *SKS*-derived FPDs. (d) The same plot for TD deviations obtained between *S*- and *SKS*-derived measurements. The color version of this figure is available only in the electronic edition.

individual *SKS* observations is small, indicating that the direct *S* measurements might be more reliable due to the larger number of contributing events. Figure 10c,d demonstrates that the deviations do not exceed 20° and 0.4 s for most of the stations when the *SKS* splitting parameters are based on more than 10 events. However, average *S* and *SKS* splitting parameters calculated by using less than seven individual events, for instance at stations H17, H18, H19, and H22, result in deviations larger than 40° (Fig. 9). There is only one station F02 with a sufficient amount of individual *SKS* and *S* observations (7 and 45, respectively) that shows a large deviation (43°). A very large deviation (i.e., 75°) was observed at the station JF020, but for this station only one *S*-wave recording from a single event was available (Fig. 9). This suggests to us that the results of our process will be fairly robust when we only accept measurements based on averaging of at least 10 events.

Bootstrap Approach

Our approach strongly depends on the robustness of known average *SKS* splitting parameters at a set of reference stations. Thus, using *SKS* splitting parameters inferred from permanent stations with a long operating period can be ad-

vantageous to ensure the reliability of knowledge of seismic anisotropy when correcting for receiver-side effects. However, in general we cannot start with a large amount of *SKS* observations. Instead, good *SKS* measurements are only available at one or a few permanent stations also operating in the area, and we want to use the direct *S* measurements to gain information about the anisotropy below stations with insufficient *SKS* measurements. We therefore establish an iterative stepwise procedure in which we start with a small number of reference stations to estimate the splitting parameters of the remaining stations. Estimates in the first step are only possible for those stations less than the threshold distance and with a sufficient number of shared events. In a second step, stations with averaged *S*-derived splitting parameters from the first iteration were added to the reference station dataset. The iterative process can be repeated to increase the number of reference stations until we reach the entire number of stations; in each iteration splitting at the reference stations is re-evaluated by treating them as target stations, too, resulting in improved splitting estimates with iteration number.

We have tested this procedure by randomly selecting 10 stations with known *SKS* splitting measurements. At the end of the first iteration, splitting estimates at 45 stations could be
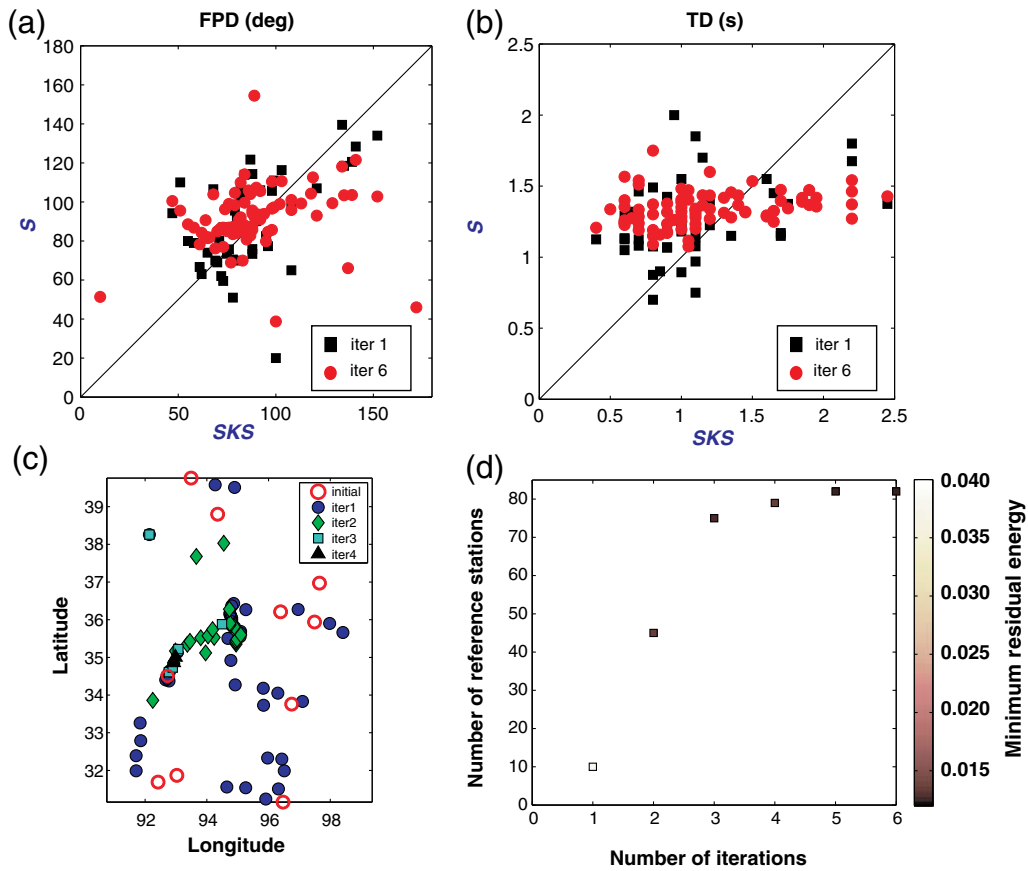
Figure 11. (a) *SKS* versus *S*-derived FPDs at iterations 1 and 6. (b) *SKS* versus *S*-derived TDs at iterations 1 and 6. (c) Location of included station as function of iteration number. (d) The number of iteration versus number of reference station at the beginning of the iteration. The minimum residual energy shown in (d) is averaged over all station–event combinations calculated at every iteration. The color version of this figure is available only in the electronic edition.

derived. In the iterative process, the average deviations between *S*-derived splitting parameters and the full *SKS* splitting parameters is larger during the first iteration compared to the case where we use all *SKS* observations (Fig. 11a,b). Figure 11c clearly displays the spatial distributions of 10 stations selected randomly at the beginning and locations of newly added stations after each iteration (in different symbols). As the number of available reference stations increases (Fig. 11c,d) in consecutive iterations the scatter becomes smaller (Figs. 11a,b) and the averaged residual energy (Fig. 11d) generally reduces, implying a better convergence to the desired minimum difference between source signals at two stations. This test has demonstrated that, with only a few stations with well-constrained *SKS* splitting results considered as seeds, it is possible to determine the splitting parameters of a large array in an iterative manner.

Discussion and Outlook

We have introduced a method to estimate the shear-wave splitting from direct *S* waves for regional arrays, which is based on matching the corrected horizontal waveforms of a reference station and a target station. This method is not af-

fected by source-side splitting, as long as the distance between the stations is small compared to the epicentral distance, such that the ray paths can be considered equivalent in the deep mantle and near the source. We have achieved good results by imposing a maximum distance of 300 km between target and reference station. The waveforms of the reference station need to be corrected first for known splitting parameters, but it is possible to start with a small number of reference stations for which splitting can be determined from *SKS* measurements—for example, a few permanent stations in the vicinity of a temporary array to seed the procedure and iteratively expand the number of reference stations. We have demonstrated by testing this bootstrap procedure using only a few *SKS* results in our case study. Care has to be taken that splitting at the selected reference stations is well constrained and that the *SKS* waveforms at the reference station can be explained by single-layer splitting.

A further underlying assumption of the method is that all the waveform differences between target and reference station are due to differences in anisotropic structure. Of course, in reality differences in isotropic structure will also cause waveform differences; for example, differences in the thickness of the crust and sedimentary layers will cause

differences in the timing and amplitude of converted phases. Kaviani *et al.* (2011) reported that strong changes in isotropic velocities within the near-surface structure may cause short scale variations in resolved *SKS* splitting parameters. However, we have found that our methodology is relatively less sensitive to shallow structure effects, even though we assumed an even larger contrast at the sediment-basement interface than did Kaviani *et al.* (2011). We have demonstrated with synthetic tests that potential biasing effects, which could result from differences in near surface or crustal structure beneath the reference and target sites, are small and remain well within the random scatter for actual observations. However, we assumed a 1D velocity structure, and if there are strong lateral heterogeneities, it is possible that estimates of anisotropy using the reference station method will be similarly biased as seen in Kaviani *et al.* (2011), who assumed a 2D velocity structure.

To further explore the influence of converted phases, we have also tested a variant of the technique, in which instead of using the horizontal components directly, we first decomposed the three orthogonal components in to *P*, *SV*, and *SH* components, according to the technique explained by Bostock (1998), and then used the *SH* and *SV* components instead of the horizontal components. This decomposition, which was carried out using theoretical back azimuths and ray parameters and near-surface velocities of 6.6 km/s for *P* wave and 3.8 km/s for *S* wave according to the IASP91 standard Earth model, should remove converted wave energy from the *SV* components under the assumption of flat-lying layers. With our data, the results with the decomposed components were very similar to the results with the horizontal components, which indicate that conversions from flat-lying layers did not substantially degrade the splitting estimates. With this test, we cannot assess the effect of scattering by 3D heterogeneities, but, similar to the arguments for the effects of scattered phases on *SKS* measurements, it is expected that the energy for the residual trace would be large if significant scattered energy were present; such a measurement would be discarded based on the maximum residual energy criterion.

Given that horizontal splitting parameters can already be determined based on *SKS* measurements; we envisage the following potential applications for the reference stations technique.

- Increase the robustness of observations by providing additional constraints, particularly where station deployment times are too short or noise levels too high to obtain more than a handful of *SKS* measurements, mostly not enough for robust estimates of shear-wave splitting. Using the bootstrap procedure it is sufficient to start with a small number of stations with well-constrained splitting parameters to obtain measurements for an expanded array.

The measurements for individual pairs are more scattered than for the classic *SKS* methods, for example, minimum-transverse energy minimization, but for each target station and event, an estimate can be derived from averaging over many pairs involving that station, and the number of direct *S* phases recorded with a good signal-to-noise ratio tends to be significantly larger than the number of well-recorded *SKS* events (for our case study, we obtained measurements from four times as many events for *S* as compared to *SKS*), such that the final estimates based on the reference station method are probably more reliable, as hinted by the observation that discrepancies between *S* and *SKS* measurements were generally largest when only very few events had contributed to the *SKS* measurement.

- Expand the range of incidence angles, back azimuths and polarizations with which the anisotropic structure is sampled. Modeling the 3D orientation of structures or multilayer splitting by using shear phases requires good incidence angles and azimuthal coverage, and with the very steep incidence angles of *SKS* waves it is generally not possible to constrain the dip of the anisotropic axis of symmetry, and the determination of the splitting parameters of double-layer splitting from *SKS* phases requires exceptionally well-distributed back azimuths. The addition of splitting measurements from *S* waves offers the potential to sample the structure with different incidence angles and thus potentially provide constraints on dipping anisotropic structures. Also, for *S* waves polarization and back azimuth are no longer coupled and thus they provide opportunities, in combination with *SKS* measurements, to obtain a much more complete sampling of polarization directions for the purpose of constraining multilayer anisotropy (Silver and Savage, 1994). However, the initial polarization might be complex due to source-side splitting, such that a detailed analysis of the best strategy for exploiting this additional information is not entirely straightforward and therefore beyond the scope of this paper. Also, to obtain robust estimates of nonhorizontal anisotropy or multilayer splitting, longer deployment times (two years or more) or exceptionally low noise levels will be required.

- Remove anisotropy-related bias from relative delay measurements for isotropic tomographic imaging. For shear-wave body-wave tomographic studies, usually the *SH* component is used to carry out relative arrival-time measurements from cross-correlation measurements. However, if we consider as an example two adjacent domains with identical average velocities, but perpendicular fast directions, and an event the back azimuth of which is aligned with the slow direction in either domain, then arrivals will appear early for stations within the domain for which the *SH* polarization is aligned with the fast direction, and late for the other domain. For another event with a back azimuth at 90° to the first-considered one, the opposite pattern will be observed. For intermediate back azimuths, the nominal *SH* component will show split fast and slow arrivals, with the results of the cross-correlation measurement affected by the exact angle and the relative amplitudes of the *SH* and *SV* field prior to entering the anisotropic medium. It is obvious that a tomographic inversion of these arrival-time
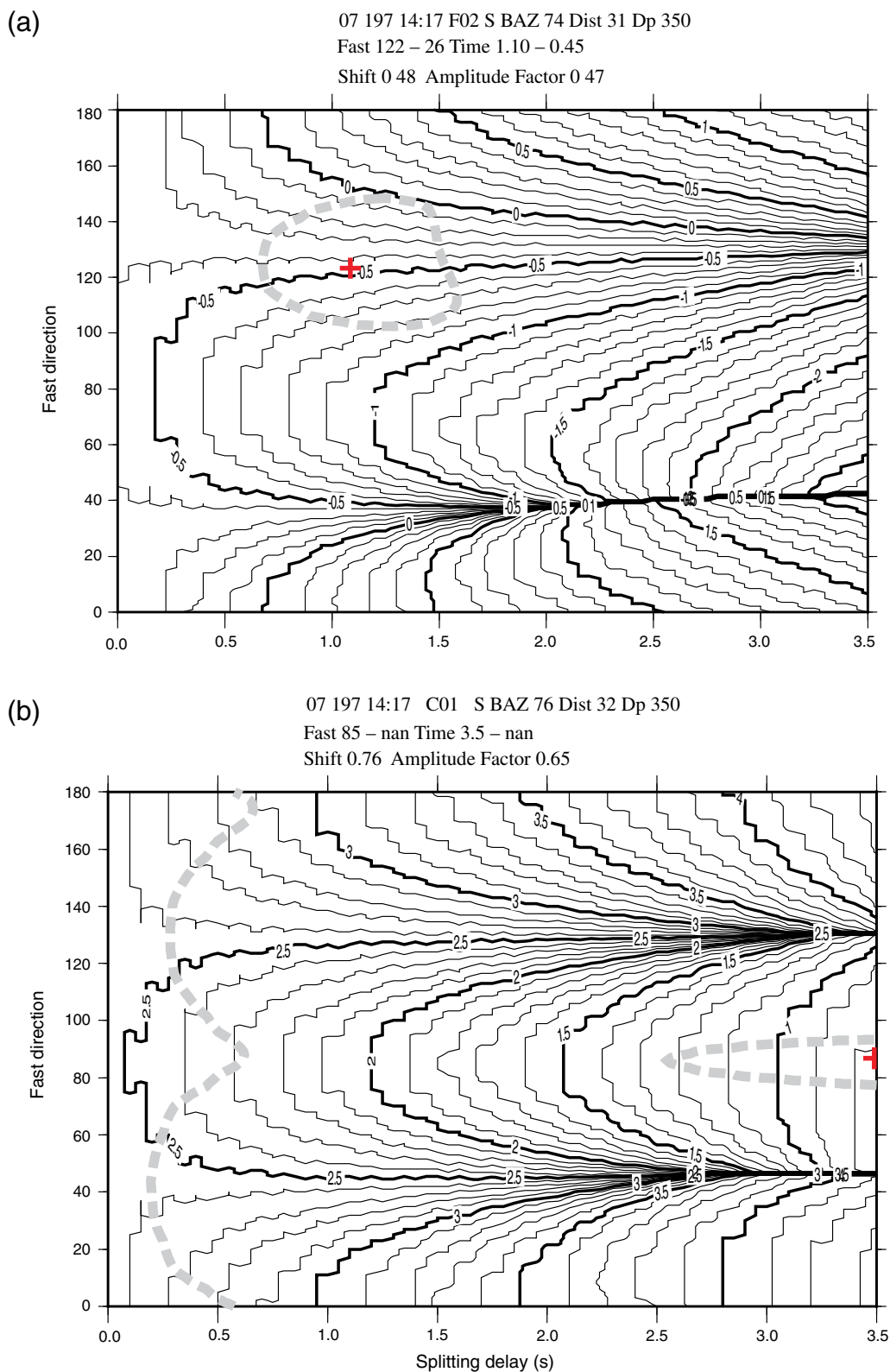
(a)

07 197 14:17 F02 S BAZ 74 Dist 31 Dp 350

Fast 122 – 26 Time 1.10 – 0.45

Shift 0 48 Amplitude Factor 0 47

(b)

07 197 14:17 C01 S BAZ 76 Dist 32 Dp 350

Fast 85 – nan Time 3.5 – nan

Shift 0.76 Amplitude Factor 0.65

Splitting delay (s)

Figure 12. Optimal delay times Δt, for all splitting parameters considered (black contours). The thick dashed contour encloses those splitting parameters within the formal 95% confidence range according to the *F*-test. A cross symbol shows splitting parameter estimate. (a) Case of well-resolved splitting (reference F01; target F02), see Figure 8a,j,e,g,i,k,m for details on the splitting measurement. (b) Null-splitting case (reference: A01; target C01), see Figure 8b,d,f,h,j,l,n. The color version of this figure is available only in the electronic edition.

measurements using an algorithm not taking into account shear-wave splitting will result in spurious heterogeneity being inferred. Yet, there will often be insufficient data for a full tomographic inversion of splitting measurements (Chevrot, 2006), and in any case the noncommutative nature of the forward splitting operator limits the applicability of simple tomographic concepts (Silver and Long, 2011). So it would be desirable to be able to measure an isotropic relative delay time, which can be used in isotropic tomographic inversions directly.

As pointed out above, the time shift Δt, which is a by-product of the reference station technique, represents just such a measurement. In Figure 12a, we have contoured the optimal values for Δt for each set of splitting parameters for the waveform pair already shown in Figure 8a,c,e,g,i,k. For the optimal splitting parameters, a time shift of -0.48 s is obtained. However, within the range of splitting parameters within the 95% confidence interval (gray contour), time shifts between -0.05 and -0.8 s are found, equivalent to a standard deviation of ~0.2 s. To further narrow the range of possible shifts from a single measurement, one could read off the time-shift value based on the splitting parameters estimated from multiple events, resulting in tighter bounds for the splitting parameters. In the null-splitting case, there is a near-perfect trade-off between splitting delay δt and time shift Δt. In this case, it is necessary to consider the information about splitting parameters obtained from other events or reference stations to obtain a meaningful delay time measurement. Again, a more detailed exploration of this application will be deferred to future publications.

Data and Resources

The waveform data were uploaded from GEOFON and the Incorporated Research Institutions for Seismology Data Management Center (IRIS-DMC) data archive system (www.iris.edu/dms/nodes/dmc, last accessed August 2012; International Federation of Digital Seismograph Networks [FDSN] network codes and year range: INDEPTH-IV XO; ASCENT: X4, both 2007–2009; http://geofon.gfz-potsdam.de/, FDSN code XO [2007–2008], restricted data, last accessed August 2013). The C++ code used for carrying out the measurements on individual pairs is available with a General Public License (GPL) license and distributed at https://github.com/ftilmann/multisplit (last accessed August 2014; see Ⓔ S1 in the electronic supplement to this article).

Acknowledgments

References

Anglin, D. K., and M. J. Fouch (2005). Seismic anisotropy in the Izu-Bonin subduction system, *Geophys. Res. Lett.* **32,** nos. 1/4, L09307, doi: 10.1029/2005GL022714.

Babuška, V., J. Plomerová, and L. Vecsey (2008). Mantle fabric of western Bohemian Massif (central Europe) constrained by 3D seismic P and S anisotropy, *Tectonophysics* **462,** 149–163.

Becker, T. W., S. Lebedev, and M. D. Long (2012). On the relationship between azimuthal anisotropy from shear wave splitting and surface wave tomography, *J. Geophys. Res.* **117,** no. B01306, doi: 10.1029/2011JB008705.

Bostock, M. G. (1998). Mantle stratigraphy and evolution of Slave province, *J. Geophys. Res.* **103,** no. B9, 21183–21200.

Chevrot, S. (2000). Multichannel analysis of shear wave splitting, *J. Geophys. Res.* **105,** 21579–21590.

Chevrot, S. (2006). Finite-frequency vectorial tomography: A new method for high-resolution imaging of upper mantle anisotropy, *Geophys. J. Int.* **165,** 641–657.

Cochran, E., J. Vidale, and Y.-G. Li (2003). Near-fault anisotropy following the Hector Mine earthquake, *J. Geophys. Res.* **10,** 2436.

Di Leo, G. F., J. Wookey, J. O. S. Hammond, J. M. Kendall, S. Kaneshima, H. Inoue, T. Yamashina, and P. Harjadi (2012). Mantle flow in regions of complex tectonics: Insights from Indonesia, *Geochem. Geophys. Geosyst.* **13,** Q12008, doi: 10.1029/2012GC004417.

Eken, T., J. Plomerová, L. Vecsey, V. Babuška, R. Roberts, H. Shomali, and R. Bodvarsson (2012). Effects of seismic anisotropy on P-velocity tomography of the Baltic Shield, *Geophys. J. Int.* **188,** 600–612, doi: 10.1111/j.1365-246X.2011.05280.x.

Eken, T., F. Tilmann, J. Mechie, W. Zhao, R. Kind, H. Su, G. Xue, and M. Karplus (2013). Seismic Anisotropy from SKS Splitting beneath Northeastern Tibet, *Bull. Seismol. Soc. Am.* doi: 10.1785/0120130054.

Fischer, K. M., and X. Yang (1994). Anisotropy in Kuril-Kamchatka subduction zone structure, *Geophys. Res. Lett.* **21,** no. 1, 5–8.

Fouch, M. J., and S. Rondenay (2006). Seismic anisotropy beneath stable continental interiors, *Phys. Earth Planet In.* **158,** 292–320.

Frederiksen, A. W., and M. G. Bostock (2000). Modelling teleseismic waves in dipping anisotropic structures, *Geophys. J. Int.* **141,** 401–412.

Iidaka, T., and F. Niu (1998). Evidence for an anisotropic lower mantle beneath eastern Asia: Comparison of shear-wave splitting data of SKS and P660s, *Geophys. Res. Lett.* **25,** 675–678.

Karato, S.-I., and P. Wu (1993). Rheology of the upper mantle: A synthesis, *Science* **260,** 771–778.

Kaviani, A., G. Rümpker, M. Weber, and G. Asch (2011). Short-scale variations of shear-wave splitting across the Dead Sea basin: Evidence for the effects of sedimentary fill, *Geophys. Res. Lett.* **38,** L04308, doi: 10.1029/2010GL046464.

Kind, R., G. Kosarev, L. Makeyeva, and L. Vinnik (1985). Observations of laterally inhomogeneous anisotropy in the continental lithosphere, *Nature* **318,** 358–361.

León Soto, G., E. Sandvol, J. F. Ni, L. Flesch, T. M. Hearn, F. Tilmann, J. Chen, and L. D. Brown (2012). Significant and vertically coherent seismic anisotropy beneath eastern Tibet, *J. Geophys. Res.* **117,** no. B5, doi: 10.1029/2011JB008919.

Levin, V., W. Menke, and J. Park (1999). Shear wave splitting in Appalachians and Urals: A case for multilayer anisotropy, *J. Geophys. Res.* **104,** 17975–17994.

Liang, X., E. Sandvol, Y. J. Chen, T. Hearn, J. Ni, S. Klemperer, Y. Shen, and F. Tilmann (2012). A complex Tibetan upper mantle: A fragmented Indian slab and no south-verging subduction of Eurasian lithosphere, *Earth Planet. Sci. Lett.* **333/334,** 101–111, doi: 10.1016/j.epsl.2012.03.036.

Lloyd, S. M., and S. van der Lee (2008). Influence of observed mantle anisotropy on isotropic tomographic models, *Geochem. Geophys. Geosyst.* **9,** Q07007, doi: 10.1029/2008GC001997.

Long, M. D. (2009). Complex anisotropy beneath D" the eastern Pacific from *SKS-SKKS* splitting discrepancies, *Earth Planet. Sci. Lett.* **283,** no. 1–4, 181–189.

Long, M. D., and R. D. van der Hilst (2005). Upper mantle anisotropy beneath Japan from shear wave splitting, *Phys. Earth Planet. In.* **151,** 206–222.

Maupin, V., E. J. Garnero, T. Lay, and M. J. Fouch (2005). Azimuthal anisotropy in the D″ layer beneath the Caribbean, *J. Geophys. Res.* **110,** no. B8, B08301, doi: 10.1029/2004JB003506.

Nunn, C., S. W. Roecker, F. J. Tilmann, K. F. Priestley, R. Heyburn, E. A. Sandvol, J. F. Ni, Y. J. Chen, and W. Zhao (2014). Imaging the lithosphere beneath NE Tibet: Teleseismic *P* and *S* body wave tomography incorporating surface wave starting models, *Geophys. J. Int.* **196,** no. 3, 1724–1741, doi: 10.1093/gji/ggt476.

O'Driscoll, L. J., E. D. Humphreys, and B. Schmandt (2011). Time corrections to teleseismic *P* delays derived from *SKS* splitting parameters and implications for western U.S. *P*-wave tomography, *Geophys. Res. Lett.* **38,** L19304, doi: 10.1029/2011GL049031.

Özalaybey, S., and M. K. Savage (1995). Shear wave splitting beneath western United States in relation to plate tectonics, *J. Geophys. Res.* **100,** 18135–18149.

Plomerová, J., V. Babuška, L. Vecsey, D. Kouba, and TOR Working Group (2002). Seismic anisotropy of the lithosphere around the Trans-European Suture Zone (TESZ) based on teleseismic body-wave data of the Tor experiment, *Tectonophysics* **360,** 89–114.

Savage, M. K. (1999). Seismic anisotropy and mantle deformation: what have we learned from shear wave splitting? *Rev. Geophys.* **37,** 65–106.

Savage, M. K., and P. G. Silver (1993). Mantle deformation and tectonics: constraints from seismic anisotropy in the western United-States, *Phys. Earth Planet. In.* **78,** 207–227.

Savage, M. K., P. G. Silver, and R. P. Meyer (1990). Observations of teleseismic shear-wave splitting in the Basin and Range from portable and permanent stations, *Geophys. Res. Lett.* **17,** no. 1, 21–24.

Silver, P. G. (1996). Seismic Anisotropy beneath the continents: Probing the depths of geology, *Ann. Rev. Earth Planet. Sci.* **22,** 385–432.

Silver, P. G., and W. W. Chan (1988). Implications for continental structure and evolution from seismic anisotropy, *Nature* **335,** 34–39.

Silver, P. G., and W. W. Chan (1991). Shear-wave splitting and subcontinental mantle deformation, *J. Geophys. Res.* **96,** no. B10, 16429–16454.

Silver, P. G., and M. D. Long (2011). The non-commutativity of shear wave splitting operators at low frequencies and implications for anisotropy tomography, *Geophys. J. Int.* **184,** 1415–1427.

Silver, P. G., and M. K. Savage (1994) The interpretation of shear wave splitting parameters in the presence of two anisotropic layers, *Geophys. J. Int.* **119,** 949–963.

Taylor, M., and A. Yin (2009). Active structure of the Himalayan-Tibetan orogen and their relationships to earthquake distribution, contemporary strain field, and Cenozoic volcanism, *Geosphere* **5,** 199–214.

Vecsey, L., J. Plomerová, and V. Babuška (2008). Shear-wave splitting measurements—Problems and solutions, *Tectonophysics* **462,** 178–196.

Vinnik, L. P., V. Farra, and B. Romanowicz (1989). Azimuthal anisotropy in the Earth from observations of SKS at Geoscope and NARS broadband stations, *Bull. Seismol. Soc. Am.* **79,** 1542–1558.

Walsh, E., R. Arnold, and M. K. Savage (2013). Silver and Chan revisited, *J. Geophys. Res.* **118,** 5500–5515, doi: 10.1002/jgrb.50386.

Wolfe, C. J., and P. Silver (1998). Seismic anisotropy of oceanic mantle: Shear wave splitting methodologies and observations, *J. Geophys. Res.* **103,** no. B1, 749–771.

Wookey, J., G. M. Kendall, and G. Barruol (2002). Mid-mantle deformation inferred from seismic anisotropy, *Nature* **415,** no. 6873, 777–780.

Yang, X., and K. M. Fischer (1994). Constraints on North Atlantic upper-mantle anisotropy from *S* and *SS* phases, *Geophys. Res. Lett.* **21,** no. 4, 309–312.

Zhao, W., P. Kumar, J. Mechie, R. Kind, R. Meissner, Z. Wu, D. Shi, H. Su, G. Xue, M. Karplus, and F. Tilmann (2011). Tibetan plate overriding the Asian plate in central and northern Tibet, *Nat. Geosci.* **4,** 870–873, doi: 10.1038/NGEO1309.

Seismology section (secion 2.4)
Deutsches GeoForschung Zentrum (GFZ)
Telegrafenberg 14473, Potsdam, Germany